Available online at www.sciencedirect.com
ScienceDirect
Trans. Nonferrous Met. Soc. China 35(2025) 3662−3676
Transactions of Nonferrous Metals Society of China
www.tnmsc.cn

Effect of TIG surface remelting on microstructure and mechanical properties of ZL109G Al alloy

Si-zhe NIU[1], Ze-long WANG[1], Zi-xuan CHEN[2,3], Ran ZONG[1], Bao-tao CHI[1], Jun WANG[4], Shi-ying LIU[4], Yun-wu MA[2,3], Shan-qing HU[5]

1. School of Mechanical Engineering, Shandong University of Technology, Zibo 255000, China;
2. State Key Laboratory of Mechanical System and Vibration, Shanghai Jiao Tong University, Shanghai 200240, China;
3. Shanghai Key Laboratory of Digital Manufacture for Thin-walled Structures, School of Mechanical Engineering, Shanghai Jiao Tong University, Shanghai 200240, China;
4. Binzhou Bohai Piston Co., Ltd., Binzhou 256602, China;
5. Institute of Materials, China Academy of Engineering Physics, Mianyang 621907, China

Received 23 February 2024; accepted 19 November 2024

Abstract: TIG surface remelting was performed to strengthen the surface of ZL109G alloy piston. The macrostructure indicates that surface remelting leads to the production of a remelted zone (RZ). The diameter of the primary Si decreases from 65.8 μm in the base metal (BM) to 7.1 μm in RZ. The grain size of the RZ is refined to be approximately one-seventh that of the BM. The cellular microstructure in the RZ is characterised by the α(Al) in the centre and intermetallics preferentially located at the cellular boundaries. The results of the mechanical properties demonstrate that the average hardness value of RZ increases by 39% compared to that of BM. For the transverse samples, the ultimate tensile strength increases by ~24.5%, which can be attributed to the solution strengthening of Si in α(Al). The average fracture toughness values are 15.0 and 12.7 MPa·m$^{1/2}$ for α(Al) in BM and RZ, respectively.

Key words: TIG surface remelting; ZL109G; microstructure refinement; tensile properties; fracture toughness

1 Introduction

Al−Si alloys are widely used for the manufacture of engine pistons because of their excellent casting performance, low density, and high-temperature mechanical properties [1−3]. Pistons operate under service conditions of severe thermal and mechanical loads with improvements in engine performance [4]. Therefore, optimizing the properties of the Al−Si alloy is necessary to improve piston performance.

For the Al−Si alloys, factors affecting the mechanical properties include the Si content and the morphology and size of the primary Si particles, α(Al), and eutectic Si particles [5,6]. RAZIN et al [7] found that the tensile strength of Al−Si alloys increased, whereas the elongation and impact energy decreased with increasing Si content. The reinforcement effect of eutectic Si particles in Al−Si alloys was thoroughly studied by ZHANG et al [8], and they found that refined and uniformly distributed eutectic Si particles enhanced the ductility of the Al−Si alloy. The effect of primary Si particles and Si-containing precipitates of Al−Si alloys on the mechanical properties was studied in detail [9,10]. The number density of nanoscale Si particles improves the mechanical properties by facilitating grain refinement and increasing dislocation density [10]. The addition of extra

Corresponding author: Si-zhe NIU, Tel: +86-15021871652, E-mail: niusizhe@sdut.edu.cn
https://doi.org/10.1016/S1003-6326(25)66905-6

elements and rapid solidification aid in optimizing the microstructure of Al−Si alloys and achieve microstructural refinement [11,12]. WU et al [13] refined α(Al) dendrites and modified Si by adding a refiner (e.g., Al−Ti−B) and modifier (e.g., Al−Sr). In addition to the modification of the Al−Si alloy matrix, various surface remelting technologies such as laser surface remelting [13−16], arc surface remelting [17], and electron beam surface remelting [18] have been applied to the Al−Si alloys. LIEN et al [19] studied the microstructure of an Al−Si alloy by laser surface remelting and found an ultrafine-scale Al−Si eutectic in the remelting zone. The sizes of the Si fibres were refined to 1.3−65 nm, and high-density nanoscale twins were formed in the Si fibres. GONG et al [20] reported that the size of the primary Si particles was reduced to 3 μm compared to the 20−30 μm of the Al−Si alloy matrix. The secondary dendrite arm spacing was 3 μm after TIG surface remelting. The surface hardness was significantly improved for the electron beam surface-remelted Al−Si alloy because of grain refinement, oversaturation of the aluminum solid solution, and enhancement of wear resistance [21].

Among the abovementioned three surface remelting technologies, the TIG surface remelting has advantages of being inexpensive, flexible, and easy to control for surface modification compared to the vacuum required for electron beam surface remelting and the high cost of laser surface remelting [22]. ORLOWICZ and MRÓZ [23] developed a stepwise regression method for Al−Si alloys to establish the relationships between the TIG surface remelting parameters and energy transfer efficiency, as well as the geometry, structure, and hardness of the fusion zone (FZ). DÖRNENBURG et al [24] applied TIG surface remelting technology to refine the primary Si in the Al−Si alloy from 50 μm in the as-cast condition to ~5 μm for the remelting condition. The fatigue lifetime increases by four times. The TIG surface remelting was conducted to strengthen the surface of the ZL109G Al−Si alloy to further analyse the microstructure evolution, fracture toughness, and strengthening mechanism after the remelting process. The microstructural characteristics, room-temperature mechanical properties, and fracture toughness were investigated in detail.

2 Experimental

2.1 Materials

The raw materials of ZL109G were cut directly from the piston parts manufactured by Shandong Binzhou Bohai Piston Co., Ltd. with thickness and diameter of 7 mm and 93 mm, respectively (Fig. 1(a)). The standard and actual chemical compositions of ZL109G are listed in Table 1.

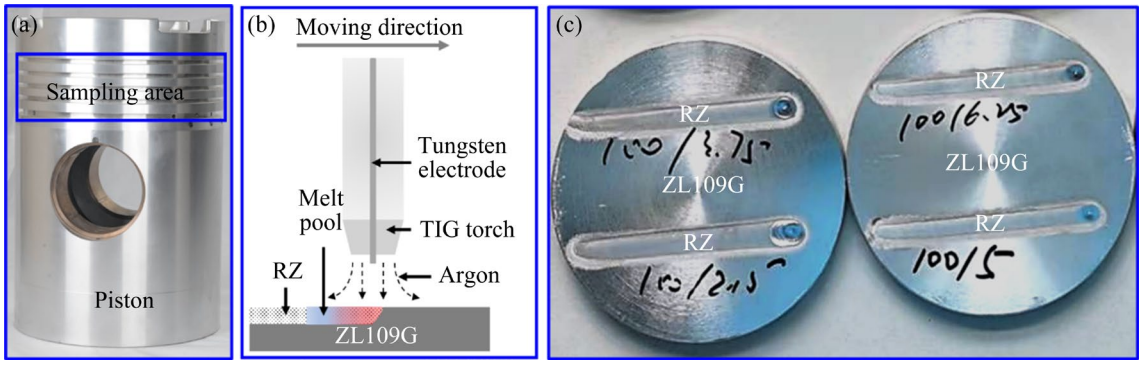

Fig. 1 Sampling area and TIG surface remelting process: (a) Sampling area; (b) Schematic of TIG surface remelting on ZL109G alloy; (c) Samples after surface remelting

Table 1 Standard and actual chemical compositions of ZL109G (wt.%)

Composition	Si	Cu	Mg	Ni	Mn	Zn	Fe	Others	Al
Standard	11−13	0.8−1.3	0.8−1.3	0.8−1.3	≤0.15	≤0.15	≤0.6	≤0.15	Bal.
Actual	12.8	1.2	0.8	1.2	0.14	0.13	0.52	−	Bal.

2.2 TIG surface remelting process

A pulsed argon arc welding machine manufactured by Shandong Aotai Electrical Ltd. (China) was used to perform TIG remelting. A schematic of the TIG surface remelting process is shown in Fig. 1(b). The TIG torch could move in a linear manner at a precise preset speed, and a 3.0 mm diameter tungsten electrode was used. The distance between the electrode and ZL109G surface was maintained at 3 mm, and the flow rate of the Ar shielding gas was 10 L/min. In the alternating current mode, the TIG surface remelting process was conducted with a current setting ranging 50−125 A at intervals of 25 A. The moving speed of the TIG torch was set from 2.5 to 6.25 mm/s at an interval of 1.25 mm/s. Figure 1(c) shows the samples remelted at 100 A.

2.3 Methods for microstructure analysis and mechanical properties testing

Metallographic samples were prepared using standard procedures. The microstructure of the cross-section of the remelted sample was observed without corrosion. Subsequently, the optical microstructure was obtained using an Olympus optical microscope (OM), and a Rigaku SmartLab SE X-ray diffraction (XRD) was used for characterising the phase compositions of the base metal (BM) and fusion zone (FZ) of the Al−Si alloy. The microstructure was characterised using an FEI Sirion 200 scanning electron microscope (SEM) equipped with an energy-dispersive spectrometer (EDS). The hardness mapping image was obtained using a Buehler Wilson VH1102 hardness tester with a force of 10 N and a dwell time of 10 s. Nano-indentation tests were performed using an MTS nanoindenter machine equipped with a Berkovich indenter, and the room-temperature tensile performance was examined using a Zwick tensile testing machine at a strain rate of 1×10^{-3} s^{-1}. The digital image correlation (DIC) technique was used to record the strain distribution. Figure 2(a) shows the sample preparation for the transverse and longitudinal tensile tests using a wire-cutting machine, and Fig. 2(b) shows the size of the tensile samples.

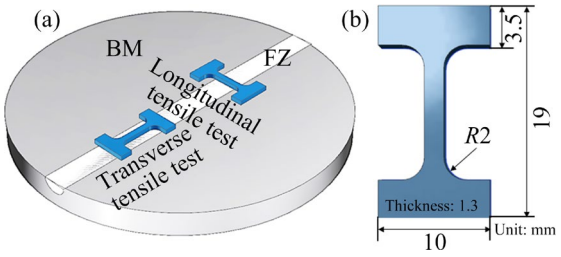

Fig. 2 Schematic of tensile test: (a) Sample preparation of transverse and longitudinal tensile tests; (b) Size of tensile samples

3 Results and discussion

3.1 Macrostructure

The heat input has a significant effect on the macromorphology of the remelting pool. As shown in Fig. 3, the section of the remelting pool has a semi-elliptical shape, and the remelted zone (RZ) decreases with reduced heat input. Further, microporosity can be clearly observed on the surface of RZ with a size of less than 300 μm. Overall, the number and size of the micropores decrease with increasing the remelting speed. Microporosity can be divided into shrinkage and gas porosity. LI et al [25] reported that shrinkage porosity caused by the solidification and shrinkage of the Al metal liquid during welding was characterised by an irregular shape, while the gas porosity caused by air trapping and undissolved hydrogen had a very round outline. Thus, micro-porosity is related to gas porosity. During TIG surface remelting, the solid-dissolved hydrogen in the BM and the hydrogen generated by H_2O decomposition at high temperatures are fused into the remelting pool. During the solidification process, the temperature drops and hydrogen precipitates to form gas pores [26]. The higher the line energy of remelting, the longer the molten pool, and the easier it is to produce gas porosity. For example, HAN et al [27] found that gas porosity appears in the laser-MIG hybrid welding of 6082-T6 Al alloy when the arc current exceeds 140 A. Consequently, improving the remelting speed can reduce the line energy and thus reduce gas porosity.

Figure 4 shows the variation in the width and height of the RZ. Both the width and height of the RZ increase with increasing current and decrease with increasing remelting speed, which can be attributed to the variations in the line energy of the remelting. The remelting samples under 100 A current were subjected to in-depth research on the microstructure and mechanical properties after comprehensive consideration of the size and defects of the RZ, as well as the convenience of follow-up research.

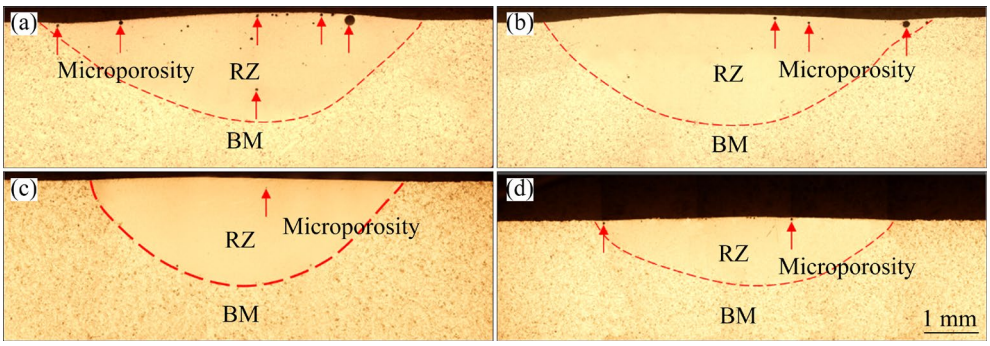

Fig. 3 Macromorphologies of remelting pool at 100 A and different remelting speeds: (a) 2.5 mm/s; (b) 3.75 mm/s; (c) 5.0 mm/s; (d) 6.25 mm/s

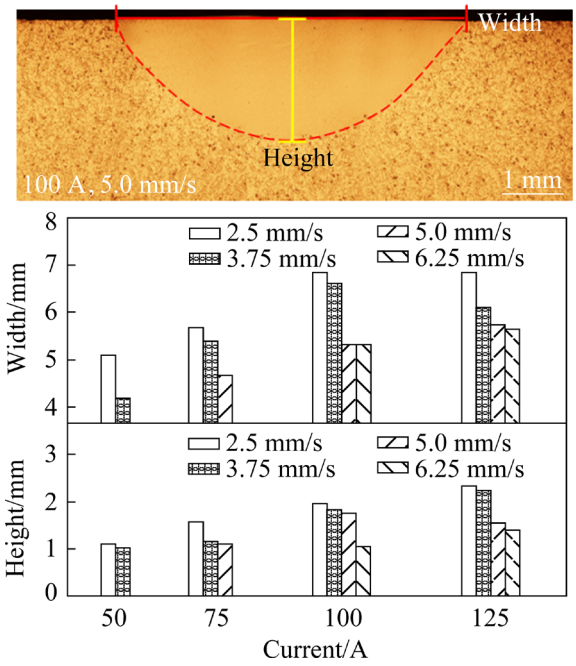

Fig. 4 Variation of RZ width and height

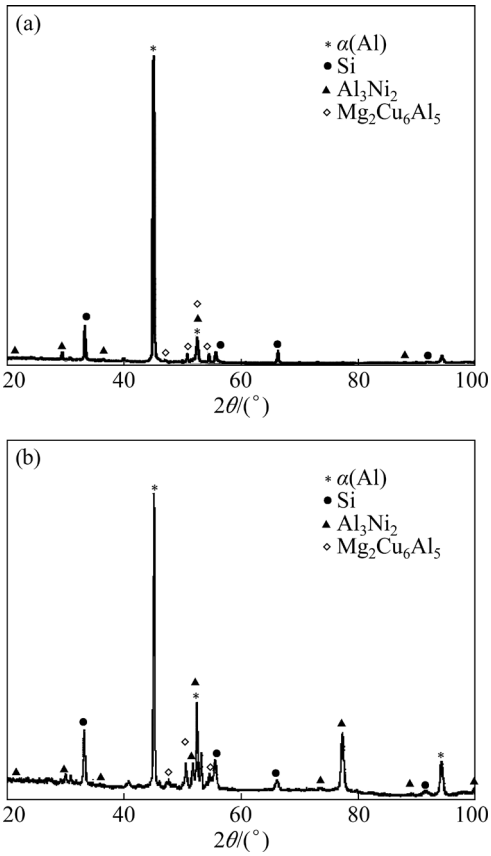

Fig. 5 Micro-XRD patterns of ZL109G BM (a) and RZ (b)

3.2 Microstructure

3.2.1 Phase composition

The micro-XRD patterns of ZL109G BM and RZ are shown in Fig. 5. The phase composition of ZL109G BM is α(Al), Si, Al_3Ni_2, and $Mg_2Cu_6Al_5$ in Fig. 5(a), and the same constituent phases can be found in RZ (Fig. 5(b)). The peak intensity of the BM is considerably higher than that of the RZ, which indicates the refined microstructure of the RZ.

3.2.2 Evolution of microstructure

Figure 6 shows the OM images of ZL109G BM and RZ. The macro morphology of the TIG-remelted samples is shown in Fig. 6(a). The microstructures are refined by comparing Figs. 6(b) and (c). For example, the diameter of the primary Si is 65.8 μm in the BM, whereas it is 7.1 μm in RZ. The amount of primary Si in RZ is considerably lower than that in BM. The cooling rate of the RZ is higher than that of the BM, which leads to a refined microstructure. Further, considering the Al−Si phase diagram, the eutectic point shifts to a higher Si content at a faster cooling rate, and the eutectic temperature is also depressed [28]. Consequently, the amount of primary Si in the RZ decreases. Figures 6(b_1, c_1), which depict the magnified microstructure in BM and RZ, respectively, present

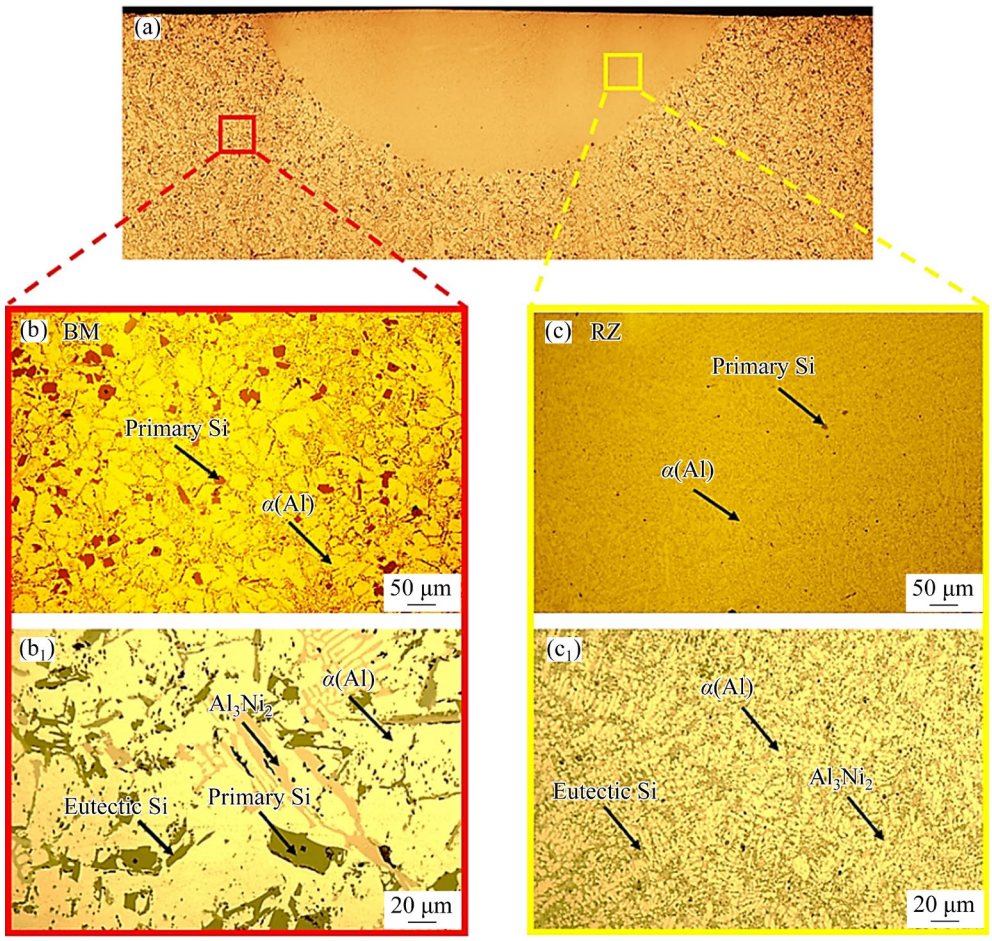

Fig. 6 OM images of ZL109G BM and RZ: (a) Macro morphology of TIG-remelted samples; (b, b_1) BM microstructure; (c, c_1) RZ microstructure

phase compositions of α(Al), primary Si, eutectic Si, and Al_3Ni_2 based on morphology and contrast. The $Mg_2Cu_6Al_5$ phase is not observed.

A typical SEM image of the TIG surface remelting-treated ZL109G alloy is shown in Fig. 7. The α(Al), primary Si, eutectic Si, Al_3Ni_2, and $Mg_2Cu_6Al_5$ phases can be found in Figs. 7(a, b). The results of the EDS point scan (Table 2) demonstrate that the brightest intermetallic phase (Point 2 in Fig. 7(b)) is $Mg_2Cu_6Al_5$, and the other is Al_3Ni_2 (Point 1 in Fig. 7(b)). The EDS results in Fig. 7(c) show that the distributions of Al, Si, Ni, and Cu are relatively concentrated, and the distribution of Mg is relatively uniform. For the SEM microstructure of the RZ, primary Si cannot be found because of its small quantity in Figs. 7(d, e). Further, cellular structures are observed in the RZ. The microstructure image reveals that the typical cellular microstructure of the TIG surface-remelted ZL109G is composed of α(Al) and intermetallics, where intermetallics are preferentially located at the cellular boundaries and α(Al) is in the centre of the cellular structure. Table 2 indicates that more Si is dissolved into the α(Al) of RZ by comparing the EDS results at Points 3 and 4 in Figs. 7(b, e). A relatively uniform distribution of all elements can be found in Fig. 7(f), which indicates that more Si elements are dissolved into the Al matrix after TIG surface remelting.

The microstructures of the interface and cellular structure are presented in Fig. 8 to clearly describe the microstructure and elemental distribution characteristics of the BM and RZ. The microstructure of the interface between BM and RZ is shown in Fig. 8(a). The results of the EDS line scan in Figs. 8(c, d) confirm that Si is more enriched in α(Al) of RZ, and Si is only enriched in primary or eutectic Si phases in BM. Figure 8(b) shows the cellular microstructure and EDS mapping results are presented in Figs. 8(e, f). The element Si tends to be distributed in α(Al), whereas the elements Cu and Ni tend to be distributed around

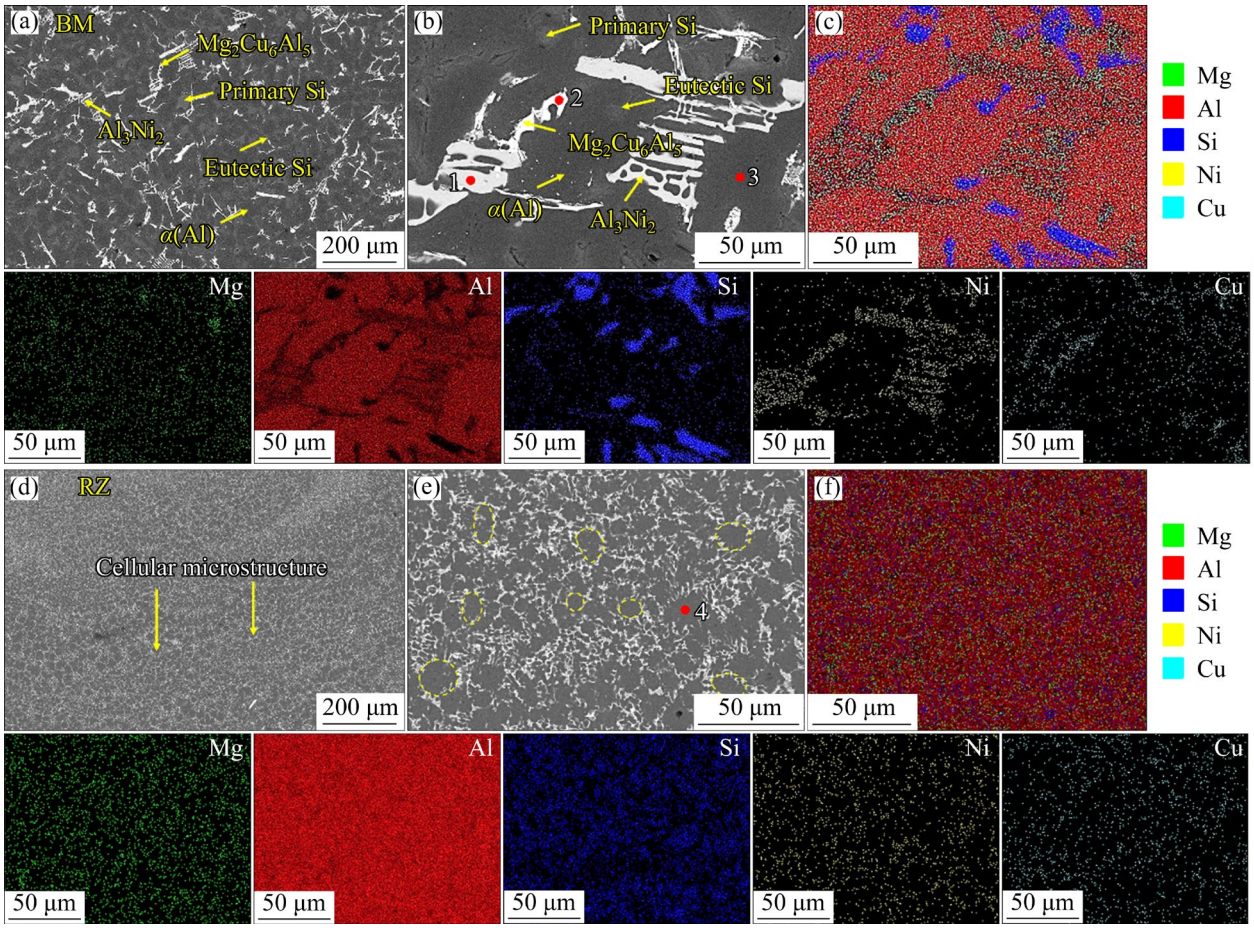

Fig. 7 Typical SEM images of ZL109G BM (a−c) and RZ (d−f): (a, d) SEM images; (b, e) Corresponding magnified SEM image and EDS point; (c, f) EDS mappings

Table 2 Results of EDS point scan in Fig. 7 (wt.%)

Point No.	Al	Mg	Si	Cu	Ni	Fe	Mn	Zn
1	65.71	0.52	1.76	1.83	22.89	6.23	0.83	0.24
2	65.05	5.46	1.67	17.20	3.38	6.16	0.83	0.25
3	91.26	1.07	5.64	1.11	0.29	0.06	0.15	0.08
4	88.16	1.11	8.61	1.03	0.49	0.19	0.20	0.21

α(Al). The average size of the cellular structure is 17.7 μm. According to the classical solidification theory, the formation of a cellular microstructure can be attributed to the minimum degree of constitutional undercooling [29]. The solute atoms are repelled to the front of the solidification interface during solidification. Cu and Ni atoms are more likely to be rejected because of the easy diffusion of Cu, which results from the low melting point and low solid solubility of Ni in Al [30]. However, the solubility of Si in Al is extended owing to the high cooling rate in the RZ after surface remelting [31], and the solute concentration in front of the solidification interface is minimised, thereby resulting in a decrease in the degree of constitutional undercooling. These are in favour of the cellular solidification kinetically, and consequently, the α(Al) solidifies first in the cellular morphology.

Variations in the grain size and morphology of the ZL109G BM and RZ are shown in Fig. 9. As shown in Fig. 9(a), the BM consists of equiaxed grains with a size of ~428 μm. After the surface remelting, the bottom of the RZ exhibits columnar

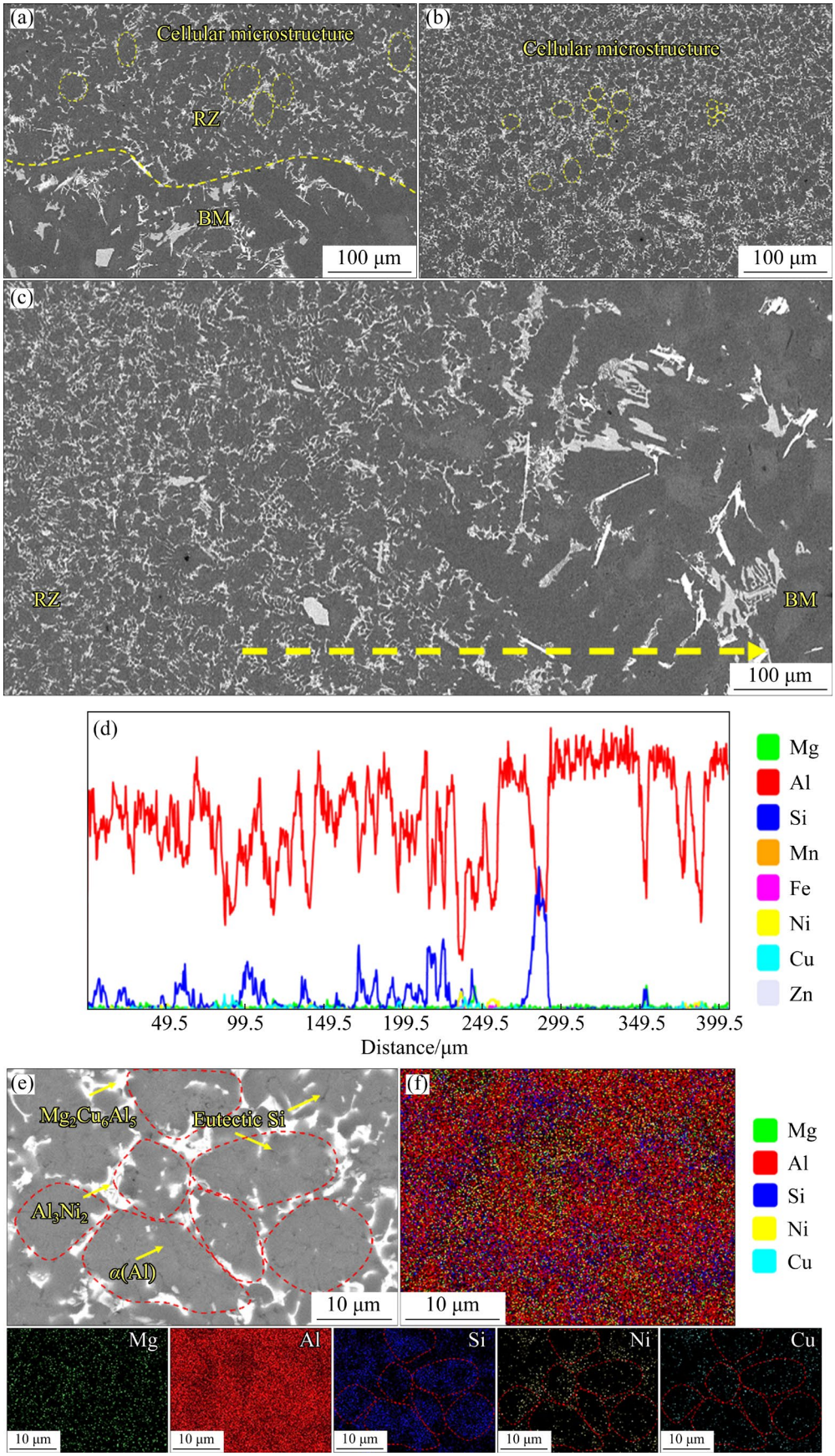

Fig. 8 Elements distribution at interface of BM and RZ, and cellular structure in RZ: (a) Microstructure characteristics at interface; (b) Cellular structure; (c, d) EDS line scan results; (e, f) Elements distribution of cellular structure

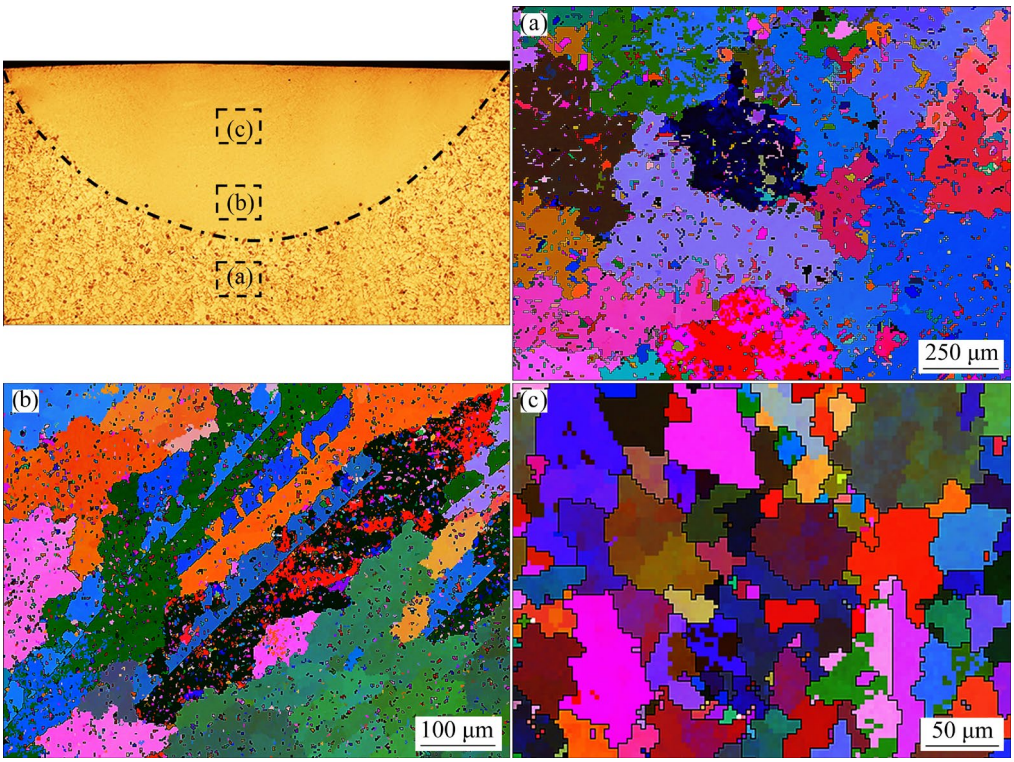

Fig. 9 EBSD Euler images showing variation of grain size and morphology of ZL109G BM and RZ: (a) BM; (b) Bottom of RZ; (c) Top of RZ

grains, as shown in Fig. 9(b), whereas the top of the RZ consists of equiaxed grains, as shown in Fig. 9(c). The average grain size of RZ is 62 μm, which is about one-seventh that of BM. Meanwhile, the columnar to equiaxed transition (CET) occurs in the RZ. WU et al [13] observed the same phenomenon for CET in the laser surface-remelted A356 Al alloy. PINEDA and MARTORANO [32] performed experiments on the solidification of Al−7%Si alloys to transform an as-cast ingot macrostructure with columnar and equiaxed grains into a completely refined equiaxed structure and concluded that a small temperature gradient and fast cooling rate could favour the formation of equiaxed grains. The phenomenon of CET in the TIG surface-remelted Al−Si alloy can be attributed to the small temperature gradient and fast cooling rate at the top of the RZ.

3.3 Mechanical properties

3.3.1 Hardness and reduced modulus

As shown in Figs. 10(a, b), the variations in hardness are similar for different remelting parameters. The average hardness value of RZ is HV 140, which is considerably higher than that of

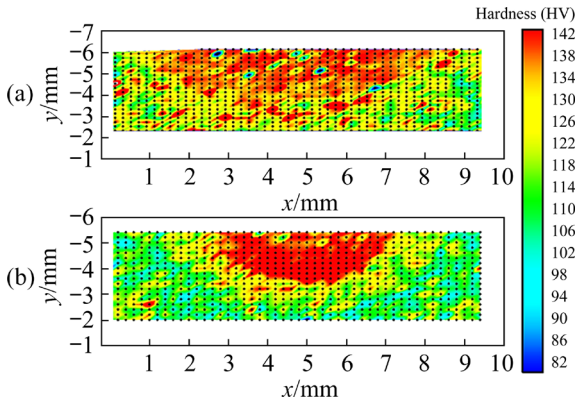

Fig. 10 Hardness distribution of TIG surface-remelted Al−Si alloy with different parameters: (a) 100 A, 3.75 mm/s; (b) 100 A, 5 mm/s

BM (HV 101), with a hardness increase of ~39%. The hardness values in BM are relatively discrete, which can be attributed to the hardness difference between the Al matrix and Si (primary and eutectic Si); the indentation did not fully cover the Al and Si phases during the hardness test. A nanoindentation test was performed to study the hardness and modulus of the different phases, and the results are presented in Figs. 11(a, b) and Table 3. The average

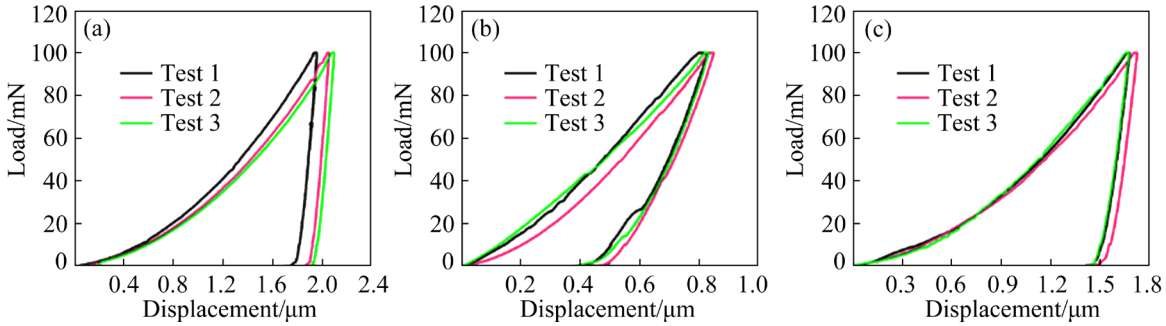

Fig. 11 Nanoindentation curves of different regions in TIG surface-remelted Al−Si alloy at 100 A and 3.75 mm/s: (a) α(Al) in BM; (b) Primary Si in BM; (c) RZ

Table 3 Results of nanoindentation hardness and reduced modulus test

Test No.	α(Al) in BM		Primary Si in BM		RZ	
	Hardness/GPa	Modulus/GPa	Hardness/GPa	Modulus/GPa	Hardness/GPa	Modulus/GPa
1	1.09	72.8	7.64	99.8	1.52	75.2
2	1.07	68.1	7.78	107.4	1.44	73.2
3	0.99	71.7	7.88	107.3	1.54	73.9
Average	1.05	70.9	7.77	104.8	1.50	74.1

nanoindentation hardness of α(Al) in BM is 1.05 GPa (HV 107), which is considerably lower than that of primary Si, which is 7.77 GPa (HV 793). Meanwhile, the average reduced modulus of primary Si (104.8 GPa) is significantly higher than that of α(Al) (70.9 GPa). After remelting, the average nanoindentation hardness of the Al matrix in RZ is 1.50 GPa (HV 153), whereas the average reduced modulus is 74.1 GPa. The nanoindentation hardness is almost consistent with the Vickers hardness. Combined with the results of the previous microstructural analysis, it can be concluded that the hardening of the RZ results from refinement of grains and solid solution strengthening.

3.3.2 Tensile properties

Figure 12 shows the stress–strain curves and DIC strain distribution of the tensile test at room temperature under surface remelting parameters of 100 A and 3.75 mm/s. The average ultimate tensile strength for the longitudinal samples is 200 MPa in Fig. 12(a), whereas it is 249 MPa in Fig. 12(b) for the transverse samples. Further, the tensile strength increases by ~24.5% after TIG remelting of the surface. Meanwhile, DIC results indicate that the distribution of strain is uniform at a strain of 0, whereas the strain in the longitudinal samples is concentrated in the BM at a strain of ~1.7%. Subsequently, the longitudinal samples are fractured in the BM. In contrast, the transverse samples fracture at strain of ~3.8%. Although the strain is not accurate because of the absence of an extensometer, the increased fracture strain for the transverse samples implies an enhancement in plasticity. Thus, it can be concluded that both the strength and plasticity are improved after TIG surface remelting of ZL109G. The evolution of the microstructure indicates that the phase composition remains the same, whereas a significant refinement of the grain size and primary Si occurs and a cellular microstructure is formed. During the surface remelting process, the primary Si is refined, transforms into eutectic Si and dissolves in the α(Al) phase. Accordingly, refined grain, solid solution, and Orowan precipitation strengthening can be used to analyse the strengthening effect of the RZ. Both grain boundaries and cellular microstructures can act as obstacles for the dislocation movement. The strengthening increment is estimated using the Hall−Patch equation [33]:

$$\Delta\sigma_{\mathrm{gb/cell}}=k\sqrt{d_{\mathrm{gb/cell}}} \quad (1)$$

where k represents the Hall–Patch coefficient for Al (k=40 MPa·μm$^{1/2}$). The grain sizes of BM and RZ are obtained from Fig. 9, and the size of the cellular microstructure is shown in Fig. 8(b). Incremental

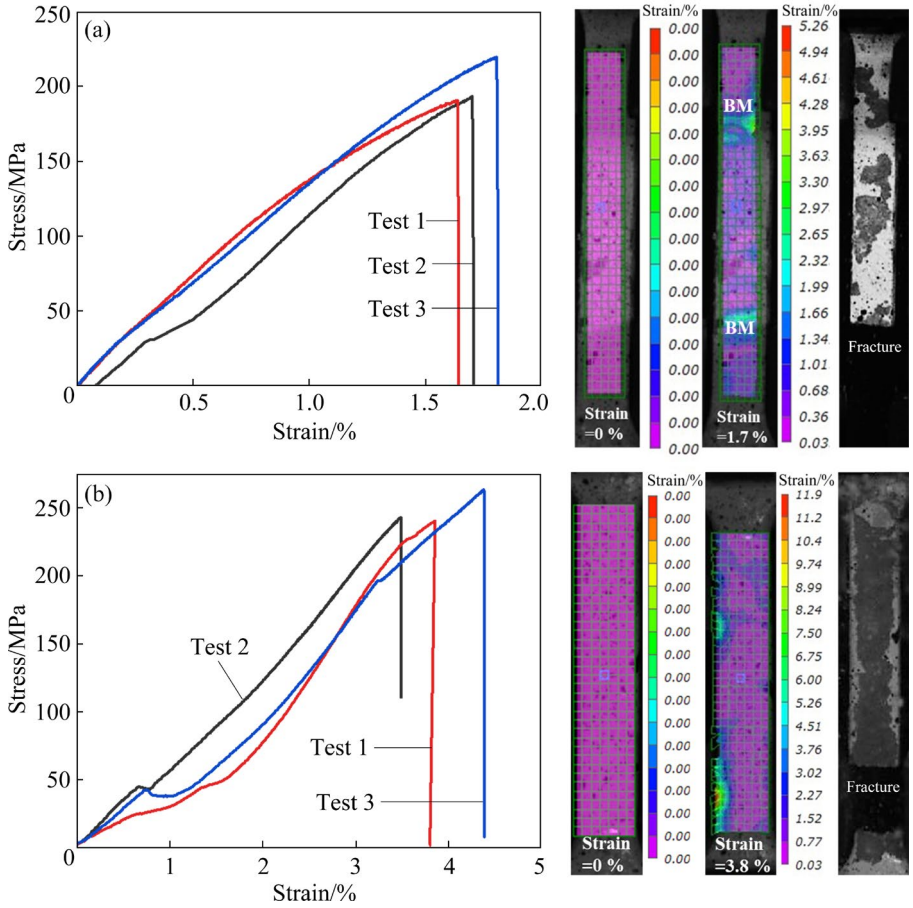

Fig. 12 Stress–strain curves and DIC strain distribution of tensile test at room temperature with surface remelting parameters of 100 A and 3.75 mm/s: (a) Longitudinal samples; (b) Transverse samples

strength of grain boundary strengthening is calculated to be 3.2 MPa, whereas that of the cellular microstructure strengthening is 9.5 MPa.

The solid solution strengthening effect of Si atoms in the α(Al) ($\Delta\theta_{ss}$) can be calculated using [33]

$$\Delta\sigma_{ss}=k_{Si}C_{Si}^{2/3} \tag{2}$$

where k_{Si} denotes the strengthening constant (39.7 MPa/wt.%$^{2/3}$) and C_{Si} represents the concentration of Si in the α(Al) matrix obtained from Table 2. The increase in solution strengthening is ~40.9 MPa.

The Orowan precipitation strengthening from the free Si ($\Delta\sigma_{Or}$) is calculated using

$$\Delta\sigma_{Or}=\frac{\varphi Gb}{d_{Si}}\left(\frac{6V_{Si}}{\pi}\right)^{1/3} \tag{3}$$

where φ (=0.4) is a material constant [34], G (=26.5 GPa) is the shear modulus of Al, and b (=0.286 nm) is the magnitude of Burgers vector of Al. Further, d_{Si} and V_{Si} are the size and volume fraction of the free Si counted from Fig. 6, respectively. The calculation results indicate that the reinforcement increment is ~0 MPa, and therefore, the total strengthening increment is ~53.6 MPa. Considering the low plasticity, the increase in the tensile strength can be attributed to the yield strength. The results of the total strengthening increment indicate that experimental results are in good agreement with the theoretical results.

Figure 13 shows the typical fracture surface morphologies of the longitudinal and transverse samples. A large cleavage plane and tearing edge exist on the fracture surface, as indicated in Figs. 13(a−c), which demonstrate that a cleavage fracture occurs in the longitudinal samples. The fracture surface of the transverse samples shown in Figs. 13(d−f) consists of small cleavages, short tearing edges, and tiny dimples, thereby suggesting that the fracture mode is a quasi-cleavage fracture.

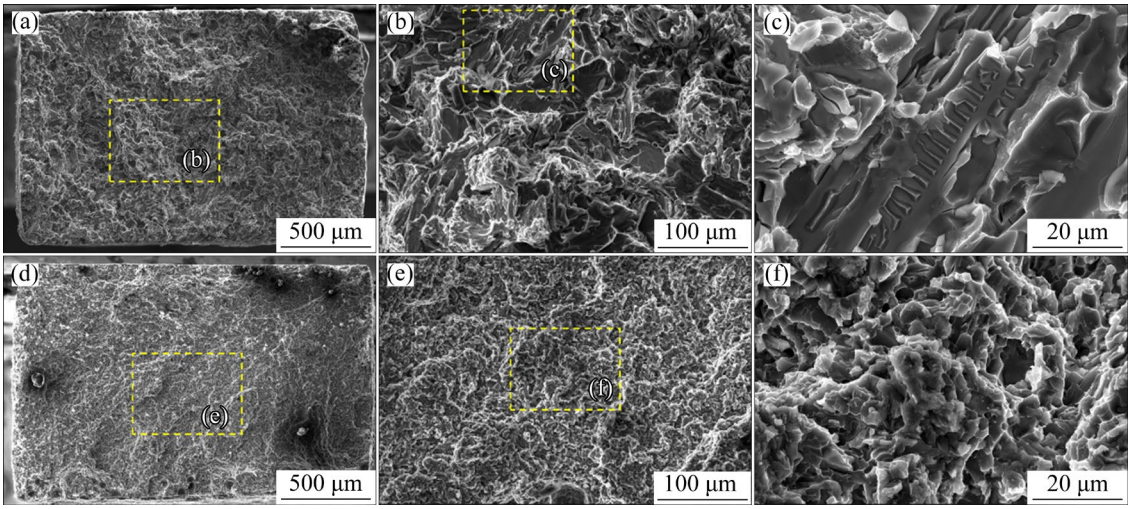

Fig. 13 Typical fracture surface morphologies: (a−c) Longitudinal samples; (d−f) Transverse samples

3.3.3 Fracture toughness

Cracks can develop in the piston because of the action of the cycle load during operation. Therefore, evaluating the fracture toughness, which indicates the resistance to crack propagation, is important. Indentation fracture mechanics is one of the most widely used methods for estimating fracture toughness [35]. In this study, the fracture toughness (K_C) of the surface-remelted ZL109G alloy is calculated using Eq. (4) and the nano-indentation method [35−37]. Only the fracture toughness of α(Al) in the BM is estimated considering the large size of free Si.

$$K_C=\sqrt{E\frac{1-\lambda\left(1+\gamma\right)\dfrac{H}{E_r}}{\dfrac{\pi}{2}\left(\tan\alpha\right)^2-\left(1-\lambda\dfrac{H}{E_r}\right)^2\tan\alpha}\frac{k'(h^*)^{n-1}}{n+1}} \tag{4}$$

where E represents the Young's modulus, λ=4.52, γ=0.27, H represents the nanoindentation hardness, E_r represents the reduced Young's modulus, tan α=2.17, k' represents the loading curve constant, n represents the loading exponent, and h^* represents the critical indentation depth.

E can be calculated using

$$\frac{1}{E_r}=\frac{\left(1-\nu^2\right)}{E}+\frac{\left(1-\nu_i^2\right)}{E_i} \tag{5}$$

where E_i (=1141 GPa) and ν_i (=0.07) are Young's modulus and Poisson's ratio of the indenter, respectively, and ν (=0.33) is the Poisson's ratio of the specimen. Further, k and n are derived by fitting the power–law relationship between the load (P) and displacement (h) of the loading curves, i.e., $P=kh^n$, as shown in Fig. 14.

The nanoindentation method could not directly determine h^*, and therefore, continuous damage mechanics (CDM) was used to estimate h^*, which can predict metal failure [38]. KACHANOV and KRAJCINOVIC [39] applied the damage variable (D) to characterise the reduction in the material mechanical properties caused by material damage. D can be estimated using

$$D=1-\frac{H_D}{H_0} \tag{6}$$

where H_D and H_0 represent the measured and average hardness values, respectively. The relationship between hardness (H_D) and displacement (h) is $H_D=A+Bh+Ch^2$, and the H_D−h curves are shown in Fig. 15.

The critical indentation depth (h^*) can be determined from the critical hardness (H_D^*) if critical hardness (H_D^*) is obtained. The damage variable (D) becomes the critical damage variable (D^*). During the nanoindentation tests, voids are generated in the material beneath the indenter under localised shear stresses. If the distribution of the voids is uniform, the critical damage variable (D^*) can be determined as

$$D^*=\frac{\pi}{\left(4\pi/3\right)^{2/3}}f^{*2/3} \tag{7}$$

Based on the CDM, a constant critical void volume fraction (f^*=0.25) [36] was used in this

study. The critical hardness (H_D^*) and critical indentation depth (h^*) were subsequently calculated.

The relative parameters of the calculations are listed in Table 4. The average K_C values are 15.0 MPa·m$^{1/2}$ for α(Al) in BM and 12.7 MPa·m$^{1/2}$ for the RZ, respectively. The chemical and phase compositions of the materials largely determine the fracture toughness [35]. Indeed, the fracture

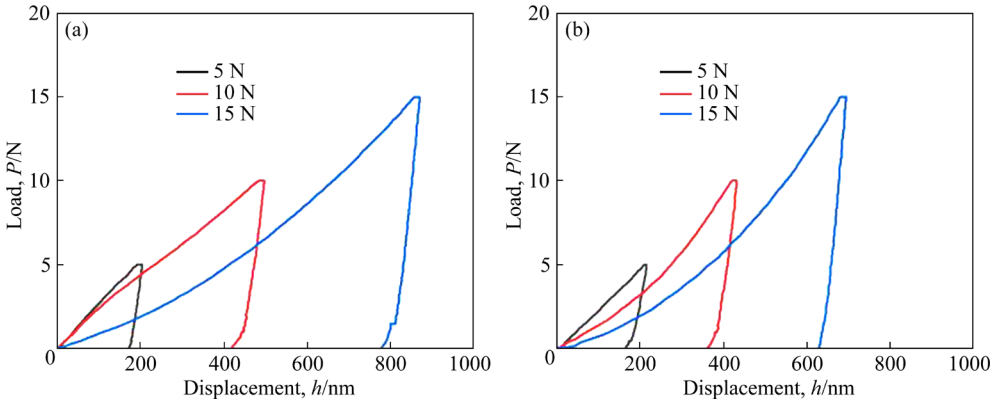

Fig. 14 Nanoindentation curves at different loads: (a) α(Al) in BM; (b) RZ

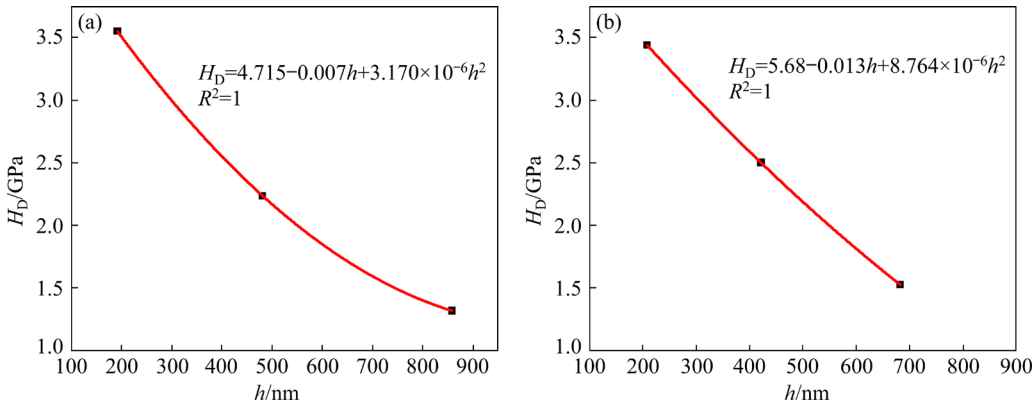

Fig. 15 H_D−h curves: (a) α(Al) in BM; (b) RZ

Table 4 Relative parameters used in process of calculation

Parameter	α(Al) in BM			RZ		
	P=5 N	P=10 N	P=15 N	P=5 N	P=10 N	P=15 N
H/GPa	3.5	2.2	1.3	3.43691	2.5	1.52729
E_r/GPa	146.4	115.1	72.8	104.9	92.9	82.0
h/nm	192.5	481.4	858.2	208.8	421.85	682.75
E/GPa	146.7	112. 4	68.7	101.6	89.16	77.96
γ	0.27	0.27	0.27	0.27	0.27	0.27
tan α	2.17	2.17	2.17	2.17	2.17	2.17
λ	4.52	4.52	4.52	4.52	4.52	4.52
k	0.0273	0.0496	0.0008	0.0167	0.0011	0.0002
n	0.9927	0.9212	1.4905	1.0661	1.5127	1.7479
H_0/GPa	2.4	2.4	2.4	2.5	2.5	2.5
H_D^*/GPa	1.3	1.3	1.3	1.3	1.3	1.3
h*/nm	881	881	881	755	755	755
K_C/(MPa·m$^{1/2}$)	17.7	16.9	10.5	14.0	13.5	10.6

toughness of α(Al) in BM with low Si solid solubility is higher than that of RZ with high Si solid solubility. The improved solid solubility and reduced grain size enhance the tensile strength of RZ in the ZL109G alloy. However, strength and plasticity are contradictory properties, and therefore, the improved solid solubility of Si inevitably reduces the plasticity of the RZ and the fracture toughness. A reduction in grain size improves both strength and plasticity; however, a smaller grain size provides less resistance to crack extension by reducing the potency of grain bridging, which lowers toughness [40].

4 Conclusions

(1) The number and size of micropores in the RZ decrease with increasing remelting speed. Both the width and height of the RZ increase with increasing current and decrease with increasing remelting speeds.

(2) The diameter of primary Si decreases from 65.8 μm in BM to 7.1 μm in RZ, and the amount of primary Si in RZ is considerably lower than that in BM. The grains size is refined from ~428 μm in BM to ~62 μm in RZ, which is about one-seventh that of BM.

(3) The EDS results show that the element Si tends to be distributed in α(Al), whereas the elements Cu and Ni tend to be distributed around α(Al).

(4) The average ultimate tensile strength for the longitudinal samples is 200 MPa, whereas it is 249 MPa for the transverse samples. The tensile strength increases by ~24.5%, which can be attributed to the solution strengthening of Si in the α(Al).

(5) The average K_C values are 15.0 MPa·m$^{1/2}$ for α(Al) in BM and 12.7 MPa·m$^{1/2}$ in RZ, indicating that the fracture toughness of α(Al) in BM with low Si solid solubility is higher than that of RZ with high Si solid solubility.

CRediT authorship contribution statement

Si-zhe NIU: Data curation, Methodology, Investigation, Writing − Original draft, Funding acquisition; **Ze-long WANG:** Methodology; **Zi-xuan CHEN:** Review; **Ran ZONG:** Methodology; **Bao-tao CHI:** Methodology, Review; **Jun WANG:** Investigation, Methodology; **Shi-ying LIU:** Supervision, Funding acquisition, Writing − Review & editing; **Yun-wu MA:** Investigation, Methodology; **Shan-qing HU:** Investigation, Methodology.

Declaration of competing interest

The authors declare that they have no known competing financial interests or personal relationships that could have appeared to influence the work reported in this paper.

Declaration of generative AI and AI-assisted technologies in the writing process

During the preparation of this work the authors used translation software in order to polish language. After using this tool/service, the authors reviewed and edited the content as needed and take full responsibility for the content of the publication.

Acknowledgments

The authors would like to acknowledge the financial support of the National Natural Science Foundation of China (Nos. 52205394, 12202251, 52305432), China, Postdoctoral Science Foundation (No. 2021M702024), Ministry of Education Industry−School Cooperative Education Project, China (No. 220606517023742), Natural Science Foundation of Shandong Province, China (No. ZR2022QE122), the Open Projects Fund of State Key Laboratory of Mechanical System and Vibration, China (No. MSV202215), and Shanghai Key Laboratory of Digital Manufacture of Thin-walled Structure, China (No. 202302).

References

[1] LIU Jiang, ZHU Xin-he, MA Deng-qing, FU Jing-guo, XUE Wen-bin, ZHANG Fan, MA Chun-sheng. Effect of nickel-coated carbon nanotubes on the preparation and wear resistance of microarc oxidation ceramic coating on ZL109 aluminum alloy [J]. Scientific Reports, 2022, 12(1): 11037.

[2] ZHOU Wei, WANG Ri-chu, PENG Chao-qun, CAI Zhi-yong. Microstructure and properties of Al−Si functionally graded materials for electronic packaging [J]. Transactions of Nonferrous Metals Society of China, 2023, 33(12): 3583−3596.

[3] WANG Zhen-hong, ZHANG Li-tong, SU Bin, ZHANG Xiao-peng. Simulation on microstructure evolution of Al−Si alloy under effect of natural convection during solidification [J]. Transactions of Nonferrous Metals Society of China, 2022, 32(1): 79−90.

[4] HAN Bing-yuan, GAO Xiang-han, CHEN Shu-ying, CONG Meng-qi, LI Ren-xing, LIU Xiao, HANG Wei-xing, CUI Fang-fang. Microstructure and tribological behavior of plasma spray Ni60 alloy coating deposited on ZL109

aluminum alloy substrate [J]. Tribology International, 2022, 175: 107859.

[5] HEKİMOĞLU A P, ÇALIŞ M, AYATA G. Effect of strontium and magnesium additions on the microstructure and mechanical properties of Al−12Si alloys [J]. Metals and Materials International, 2019, 25: 1488−1499.

[6] HEKİMOĞLU A P, HACIOSMANOĞLU M. Effect of copper and magnesium additions on the structural, mechanical and tribological properties of the Al−17Si alloy [J]. Journal of Engineering Research and Development, 2019, 11(2): 685−694.

[7] RAZIN A A, AHAMMED D S-S, KHAN A A, KAISER M S. Dissimilarity of physical and mechanical properties of Al−(0.2−17.9)wt.%Si automotive alloys in under ageing, peak ageing, and over ageing conditions [J]. Materials Today: Proceedings, 2023, 82: 248−254.

[8] ZHANG X, HUANG L K, ZHANG B, CHEN Y Z, DUAN S Y, LIU G. YANG C L, LIU F. Enhanced strength and ductility of A356 alloy due to composite effect of near-rapid solidification and thermo-mechanical treatment [J]. Materials Science and Engineering A, 2019, 753, 168−178.

[9] ZHANG Yong, ZHENG Hong-liang, LIU Yue, SHI Lei, XU Rong-fu, TIAN Xue-lei. Cluster-assisted nucleation of silicon phase in hypoeutectic Al−Si alloy with further inoculation [J]. Acta Materialia, 2014, 70: 162−173.

[10] ZHANG X, HUANG L K, ZHANG B, CHEN Y Z, LIU F. Microstructural evolution and strengthening mechanism of an Al−Si−Mg alloy processed by high-pressure torsion with different heat treatments [J]. Materials Science and Engineering A, 2020, 794: 139932.

[11] FERRARINI C F, BOLFARINI C, KIMINAMI C S, BOTTA F W J. Microstructure and mechanical properties of spray deposited hypoeutectic Al−Si alloy [J]. Materials Science and Engineering A, 2004, 375/376/377: 577−580.

[12] LI J H, WANG X D, LUDWIG T H, TSUNEKAWA Y, ARNBERG L, JIANG J Z, SCHUMACHER P. Modification of eutectic Si in Al−Si alloys with Eu addition [J]. Acta Materialia, 2015, 84: 153−163.

[13] WU Da-yong, LI Song, MA Si-da,WANG Li-sheng, KANG Jie, DONG Hui-cong, WANG Qian, WANG Yan-dong, SU Ru. Multi-scale investigation of A356 alloy with trace Ce addition processed by laser surface remelting [J]. Materials Characterization, 2022, 188: 111895.

[14] BUKHARI S M A, HUSNAIN N, SIDDIQUI F A, ANWAR M T, KHOSA A A, IMRAN M, QURESHI T H, AHMAD R. Effect of laser surface remelting on microstructure, mechanical properties and tribological properties of metals and alloys: A review [J]. Optics & Laser Technology, 2023, 165: 109588.

[15] ZHANG Cheng-quan, CHAI Lin-jiang, LI Qi-qi, MA Yan-long, WANG Hui, AN Xu-guang. Effect of scanning speed on microstructure and texture of laser surface remelted 1050 Al alloy [J]. Transactions of Nonferrous Metals Society of China, 2023, 33(6): 1677−1686.

[16] ZHANG Cheng-quan, CHAI Lin-jiang, LIU Yuan-zhuo, Li Zhi-hao, ZHANG Fang-li, LI Xin-yi, FU Zhong-tao. Correlating microstructural features with improved wear and corrosion resistance of laser surface remelted A356 alloy at different scanning speeds [J]. Materials Characterization, 2023, 202: 113021.

[17] HEKİMOĞLU A P, ÇALIŞ M. Effect of arc re-melting on microstructure, mechanical and tribological properties of commercial 390A alloy [J]. Transactions of Nonferrous Metals Society of China, 2021, 31(8): 2264−2276.

[18] JUNG A, BUCHWALDER A, HEGELMANN E, HENGST P, ZENKER R. Surface engineering of spray-formed aluminium-silicon alloys by plasma nitriding and subsequent electron beam remelting [J]. Surface and Coatings Technology, 2018, 335: 166−172.

[19] LIEN H, MAZUMDER J, WANG Jian, MISRA A. Microstructure evolution and high density of nanotwinned ultrafine Si in hypereutectic Al−Si alloy by laser surface remelting [J]. Materials Characterization, 2020, 161: 110147.

[20] GONG Zhuo, ZHANG Guo-dong, ZHENG Fei, WEN Zhi-gao, PENG Ming-cheng. Performance of different TIG remelting processes in hypereutectic Al−Si cast alloy [J]. Engineering Research Express, 2019, 1(2): 025027.

[21] HEGELMANN E, JUNG A, HENGST P, ZENKER R, BUCHWALDER A. Investigations regarding electron beam surface remelting of plasma nitrided spray-formed hypereutectic Al−Si Alloy [J]. Advanced Engineering Materials, 2018, 20(9): 1800244.

[22] MITELEA I, BORDEAŞU I, FRANT F, UŢU I, CRĂCIUNESCU C M, GHERA C. Cavitation erosion characteristics of the EN AW-6082 aluminum alloy by TIG surface remelting [J]. Materials (Basel), 2023, 16(7): 2563.

[23] ORLOWICZ A W, MRÓZ M. Study on susceptibility of Al−Si alloy castings to surface refinement with TIG arc [J]. International Journal of Materials Research, 2005, 96(12): 1391−1397.

[24] DÖRNENBURG F, LADES K, KENNINGLEY S. New technique for increasing the high-temperature durability of aluminium pistons [J]. MTZ worldwide, 2010, 71(4): 18−21.

[25] LI Zi-xin, JING Yu-hai, GUO Hong-min, SUN Xiu-yuan, YU Kun, YU An-shan, JIANG Xing-wang, YANG X J. Study of 3D pores and its relationship with crack initiation factors of aluminum alloy die castings [J]. Metallurgical and Materials Transactions B, 2019, 50(3): 1204−1212.

[26] ARDIKA R D, TRIYONO T, MUHAYAT N, TRIYONO. A review porosity in aluminum welding [J]. Procedia Structural Integrity, 2021, 33: 171−180.

[27] HAN Xiao-hui, YANG Zhi-bin, MA Yin, SHI Chun-yuan, XIN Zhi-bin. Porosity distribution and mechanical response of laser-MIG hybrid butt welded 6082-T6 aluminum alloy joint [J]. Optics & Laser Technology, 2020, 132: 106511.

[28] MAKHLOUF M M, GUTHY H V. The aluminum–silicon eutectic reaction: Mechanisms and crystallography [J]. Journal of Light Metals, 2001, 1(4): 199−218.

[29] KOU S. Welding metallurgy [M]. 2nd ed. New York: John Wiley & Sons, Inc, 2003.

[30] DENG Jun-wang, CHEN Chao, LIU Xiao-chun, Li Yun-ping, ZHOU Ke-chao, GUO Sheng-min. A high-strength heat-resistant Al−5.7Ni eutectic alloy with spherical Al_3Ni nano-particles by selective laser melting [J]. Scripta Materialia, 2021, 203(4): 114034.

[31] PRASHANTH K G, SCUDINO S, KLAUSS H J, SURREDDI K B, LÖBER L, WANG Z, CHAUBEY A K,

KÜHN U, ECKERT J. Microstructure and mechanical properties of Al−12Si produced by selective laser melting: Effect of heat treatment [J]. Materials Science and Engineering A, 2014, 590: 153−160.

[32] PINEDA D A, MARTORANO M A. Columnar to equiaxed transition in directional solidification of inoculated melts [J]. Acta Materialia, 2013, 61: 1785−1797.

[33] WANG R, WANG J, LEI L M, YU S, HU T, SHUAI S S, XU S Z, CAO Z H, LI X P, CHNE C Y, REN Z M. Laser additive manufacturing of strong and ductile Al−12Si alloy under static magnetic field [J]. Journal of Materials Science & Technology, 2023, 163: 101−112.

[34] CYR E D, BRAHME A, MOHAMMADI M, MISHRA R K, INAL K. A new crystal plasticity framework to simulate the large strain behavior of aluminum alloys at warm temperatures [J]. Materials Science and Engineering A, 2018, 727: 11−28.

[35] GÜNEN A, MAKUCH N, ALTINAY Y, ÇARBOĞA C, DAL S, KARACA Y. Determination of fracture toughness of boride layers grown on $Co_{1.21}Cr_{1.82}Fe_{1.44}Mn_{1.32}Ni_{1.12}Al_{0.08}B_{0.01}$ high entropy alloy by nanoindentation [J]. Ceramics International, 2022, 48(24): 36410−36424.

[36] LEE J S, JANG J I, LEE B W, CHOI Y, LEE S G, KWON D. An instrumented indentation technique for estimating fracture toughness of ductile materials: A critical indentation energy model based on continuum damage mechanics [J]. Acta Materialia, 2006, 54: 1101−1109.

[37] GUO H, JIANG C B, YANG B J, WANG J Q. On the fracture toughness of bulk metallic glasses under Berkovich nanoindentation [J]. Journal of Non-Crystalline Solids, 2018, 481: 321−328.

[38] HE Min, LI Fu-guo, ALI N. A normalized damage variable for ductile metals based on toughness performance [J]. Materials Science and Engineering A, 2011, 528: 832−837.

[39] KACHANOV L M, KRAJCINOVIC D. Introduction to continuum damage mechanics [J]. Journal of Applied Mechanics, 1986, 54(2): 481.

[40] LAUNEY M, RITCHIE R. On the fracture toughness of advanced materials [J]. Advanced Materials, 2009, 21(20): 2103−2110.

TIG 表面重熔对 ZL109G 铝合金显微组织和力学性能的影响

牛嗣哲[1]，王泽龙[1]，陈子轩[2,3]，宗 然[1]，池宝涛[1]，王 君[4]，刘世英[4]，马运五[2,3]，胡珊青[5]

1. 山东理工大学 机械工程学院，淄博 255000；
2. 上海交通大学 机械系统与振动全国重点实验室，上海 200240；
3. 上海交通大学 机械与动力工程学院 薄板结构数字化制造重点实验室，上海 200240；
4. 滨州渤海活塞有限公司，滨州 256602；
5. 中国工程物理研究院 材料研究所，绵阳 621907

摘 要：采用 TIG 表面重熔工艺对 ZL109G 合金活塞表面进行强化处理。宏观结构研究表明：表面重熔产生重熔区(RZ)，初生 Si 的直径从母材(BM)的 65.8 μm 减小到重熔区的 7.1 μm，重熔区的晶粒尺寸细化至母材的 1/7 左右。在重熔区中发现了胞状组织，其特征是 α(Al)位于胞状组织的中心，金属间化合物倾向分布于胞状结构边界。力学性能测试结果表明，重熔区的平均硬度比母材提高了 39%；横向试样的抗拉强度提高了约 24.5%，这主要归因于 Si 在 α(Al)中的固溶强化；母材和重熔区中 α(Al)的平均断裂韧性值分别为 15.0 MPa·m$^{1/2}$ 和 12.7 MPa·m$^{1/2}$。

关键词：TIG 表面重熔；ZL109G；显微组织细化；拉伸性能；断裂韧性

(Edited by Bing YANG)